Structural evolution induced by acceptor doping into BaTiO₃ ceramics

X.K. Wei, Q.H. Zhang, F.Y. Li, C.Q. Jin, R.C. Yu*

Beijing National Laboratory for Condensed Matter Physics, Institute of Physics, Chinese Academy of Sciences, Beijing 100190, PR China

ARTICLE INFO

ABSTRACT

Solid state reaction method is used to synthesize $Ba(Ti_{1-x}TM_x)O_{3-\delta}$ (TM = Fe, Mn and Co) and $(Ba_{1-y}Sr_y)(Ti_{1/3}Fe_{2/3})O_{3-\delta}$ ceramics. The X-ray diffraction, scanning electron microscopy and transmission electron microscopy investigations reveal that structural evolutions from an orthorhombic BaTiO₃ to a hexagonal $Ba(Ti_{1-x}TM_x)O_{3-\delta}$, a hexagonal to a rhombohedral in $Ba(Ti_{1-x}Mn_x)O_{3-\delta}$, and a hexagonal to a pseudo-cubic transition in $(Ba_{1-y}Sr_y)(Ti_{1/3}Fe_{2/3})O_{3-\delta}$ are induced by increasing the doping concentration. Due to the oxygen vacancies derived from acceptor doping, nanoscale domains of incommensurate modulation (ICM) resultant are commonly observed in the hexagonal $Ba(Ti_{1-x}TM_x)O_{3-\delta}$ compounds. The newly discovered rhombohedral $Ba(Ti_{1/3}Mn_{2/3})O_{3-\delta}$ having characteristic of face-sharing prism corner-connected by oxygen atoms is a typical example in searching for novel multiferroics. Discrepancies between the ionic radii of the B- and A-site dopants and that of Ti and Ba as a function of the doping concentrations, i.e., the effects of oxygen vacancies and the electronic configurations of the dopants, are concluded to be the driving forces for the structural transitions.

1. Introduction

The magnetoelectric multiferroics, in which the ferromagnetism and ferroelectricity coexist, is becoming more and more attractive in recent years because of the potential applications in multiple state memory elements, magnetic valve, filtering device, etc. [1,2]. In spite that many magnetoelectrics with strong coupling interactions have been discovered, BiFeO₃ is the unique single-phase magnetoelectrics with ferroelectric Curie temperature (∼820 °C) and antiferromagnetic Neél temperature (∼370 °C) above room temperature [3]. As an alternative attempt to search for room temperature magnetoelectrics, the substitution of B-site d⁰ cations in ferroelectric perovskite oxides by magnetic dⁿ cations was revitalized recently. Take $Ba(Ti_{1-x}Fe_x)O_{3-\delta}$ as an example, coexistence of room temperature ferroelectricity and ferromagnetism was revealed in a tetragonal polymorph [4–6]. Room temperature ferromagnetism was also realized in the transition-metal doped hexagonal polymorph [7–10].

As an effective approach in altering or modifying physical properties, doping into ABO₃ compounds at A-site or B-site is widely used. Recent investigations on the microstructure and magnetic properties of K/Sr and Fe codoped BaTiO₃ reveal that room tem-

perature ferromagnetism was achieved by annealing [11,12]. This means that transition-metal doped $(Ba_{1-x}Sr_x)TiO_3$ (BST), which has been one of the most promising materials for practical use in the capacitor of giga-bit dynamic random access memories [13], will be good candidates for multiferroic research. Furthermore, enhanced ferroelectric properties of Fe-doped BaTiO₃ thin film are also reported in Ref. [14]. It should be noted that the variations of electronic structure of the host elements induced by the dopants will play a dominant role in the magnetic and ferroelectric behaviors of the doped system. The giant dielectric permittivity observed in Li and Ti doped NiO is a good example [15].

Meanwhile, structural phase transition caused by doping will help us to synthesize new compounds, whose room temperature magentoelectric effect can be expected owing to the novel physical properties and the origin mechanisms of the ferroic orders. As the ferroelectricity revealed in DyMn₂O₅ [16] and YMnO₃ [17], in which the asymmetric pyramidal coordination plays an important role, the control of the oxygen vacancy location may bring about the varied coordination and subsequently the possible novel multiferroics [18]. In view of the situations mentioned above, by means of replacing Ti by Fe, Mn and Co in BaTiO₃ and Sr doping into A-site of $Ba(Ti_{1/3}Fe_{2/3})O_{3-\delta}$, new compounds are explored in the form of structural evolution in this paper. In addition to the nanoscale domains coming from structural incommensurate modulation (ICM) in the 6H-type compounds, rhombohedral $Ba(Ti_{1/3}Mn_{2/3})O_{3-\delta}$ (isostructural to BaFeO₃ with a space group of

---

* Corresponding author. Tel.: +86 10 82649159; fax: +86 10 82649531.
E-mail address: rcyu@aphy.iphy.ac.cn (R.C. Yu).
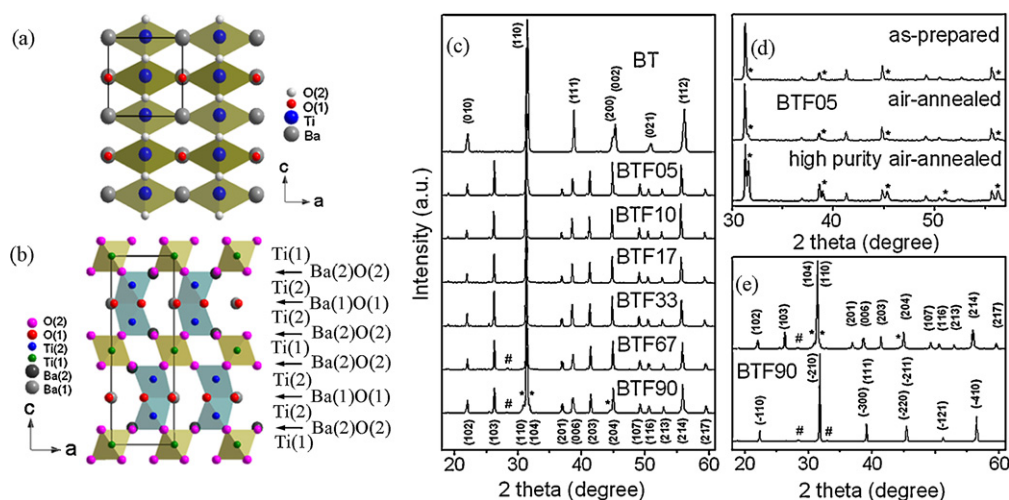
Fig. 1. (a and b) The schematic crystal structures of orthorhombic and hexagonal BaTiO$_3$ viewing along [0 1 0] zone axis. (c) The XRD patterns of Ba(Ti$_{1-x}$Fe$_x$)O$_{3-\delta}$ ceramics, wherein, BTF10 is synthesized first in oxygen atmosphere at 1000 °C (20 h), then 1350 °C (20 h) and post-annealed at 1300 °C (20 h) in air. (d) The XRD patterns of the as-prepared, air-annealed and high purity reactants synthesized BTF05, which is first sintered at 1000 °C (20 h) in oxygen atmosphere, then sintered at 1300 °C (20 h) and finally annealed at 1250 °C (20 h) in air. (e) The XRD patterns of two polymorphs of BTF90. The symbols # and * denote structures being isostructural with BaFe$_2$O$_4$ and BaFe$_{0.72}$Fe$_{0.28}$O$_{2.64}$, respectively.

$R\bar{3}m$) characterized by face-sharing prism corner-connected by oxygen atoms is discovered. As the structural evolution from the tetragonal to the hexagonal revealed in transition-metal doped BaTiO$_3$ [10,19] and Sr-doped Ba(Ti$_{0.3}$Fe$_{0.7}$)O$_3$ [20], the reason for the stabilization of the hexagonal phase due to acceptor doping is discussed.

2. Experimental details

Samples were prepared with traditional solid state reaction method from stoichiometric quantities of cabonates and oxides of the different constituents according to the general formula (Ba$_{1-y}$Sr$_y$)(Ti$_{1-x}$TM$_x$)O$_{3-\delta}$, where TM = Fe, Mn and Co. The Sr was merely doped into Ba(Ti$_{1/3}$Fe$_{2/3}$)O$_{3-\delta}$, in which the ratio of B-site Ti/Fe was fixed at 1/2. The BaCO$_3$, TiO$_2$, Mn$_2$O$_3$ and Co$_2$O$_3$ with purities of ≥99.0% as well as Fe$_2$O$_3$ (≥99.99%) were used in our experiments. High purity BaCO$_3$ and TiO$_2$ (≥99.99%) were used in Fe-doped case in order to figure out the purity influence to the polymorph. Thoroughly grinding and pellet pressing (10 mm in diameter and ~1.5 mm thick) were performed prior to each step of sintering. Most samples were sintered at 1300 °C (20 h) after the preliminary sintering (1100 °C (20 h)). Then post-annealing at 1100 °C (20 h) or third time sintering at 1300 °C (20 h) was carried out. Additional sintering conditions for some other samples will be given in the text.

The X-ray diffraction (XRD) experiments were carried out on Philips X'Pert PRO powder diffractometer (Cu Kα_1 = 1.5406 Å) with a scan step of 0.017, and the data refinement was performed with Rietveld method on FullProf software package. An XL30 S-FEG scanning electron microscope (SEM) (FEI) with an accelerating voltage of 10 kV and a transmission electron microscope (TEM) equipped with a field emission gun operated at 200 kV were used to characterize their morphology and structure features, respectively. Specimens for TEM observations were prepared by mechanically polishing then ion milling or crushing the sample in ethanol into fine fragments then supporting them on carbon film covered copper grid.

3. Results

3.1. Orthorhombic to hexagonal transition in Ba(Ti$_{1-x}$Fe$_x$)O$_{3-\delta}$ ceramics

Fig. 1(a) and (b) shows the schematic crystal structures of orthorhombic BaTiO$_3$ (o-BT) and 6H-hexagonal BaTiO$_3$ (h-BT), respectively. In order to figure out the doping limit and in consideration of the B-site atom ratio M2/M1 = 2 (M1 and M2 are two different occupations at B-site in the 6H polymorph) in the hexagonal phase, x = 0, 1/18, 1/10, 1/6, 1/3, 2/3 and 9/10 are chosen in Ba(Ti$_{1-x}$Fe$_x$)O$_{3-\delta}$, which are abbreviated as BT, BTF05, BTF10, BTF17, BTF33, BTF67, BTF90, respectively, and the XRD patterns are shown in Fig. 1(c). The BT forms an orthorhombic phase ($a \approx 4.02(6)$, $b \approx 4.00(6)$ and $c \approx 3.99(6)$ Å; $\alpha = \beta = \gamma = 90°$)

(space group $Amm2$), and a pure hexagonal polymorph (space group $P6_3/mmc$) is obtained when 1/10 Fe is doped. The pure hexagonal phase is not acquired in x = 1/18 doped BT matrix in our experiments. Studies on doping limit in BaTiO$_3$ were also performed by other groups [21,22]. As Fig. 1(d) exhibits, post-annealing in air does not eliminate the coexisted rhombohedral phase. The BTF05 synthesized with high purity reactants highlights increase of the amount of the secondary phase. It is concluded that the adoptable doping range is from 1/10 to 7/10 [22,23], nevertheless, amount of chemical bond breaking induced by high concentration of acceptor incorporation substantially alters the microscopic structure of the doping system. Furthermore, the general expansion of cell parameters in the oxygen vacancy abundant hexagonal phases [21,24] seems to be failed in our experiments (see Fig. 1(c)). Details on these two points will be discussed later. The stable bulk hexagonal compound with x = 1/2 is almost absent, but Grey et al. [21] reported a sub-stable phase obtained by quenching the sample in liquid nitrogen or slow cooling it in oxygen atmosphere.

When doping concentrations get close to the high concentration limit, a secondary phase isostructural with an orthorhombic BaFe$_2$O$_4$ [9] often occurs, as the peak at $2\theta \approx 28.3°$ denoted on BTF67 and BTF90 in Fig. 1(c). Post-annealing in air at high temperature, e.g., 1100 °C, is an effective approach to avoid it. In order to offset the excessive chemical imbalance, tetravalent Fe usually comes into being when doping concentration becomes higher than x = 8/10 [6,21]. In this high doping region, temperature, atmosphere and even humidity, etc. are crucial factors in getting the expected polymorph [21,22,25]. Take BTF90 for example, the hexagonal phase is obtained at the sintering temperature of 1300 °C (20 h × 2) in air while a monoclinic phase ($a \approx 6.92(9)$, $b \approx 4.89(8)$, $c \approx 2.82(2)$ Å, $\alpha = \gamma = 90°$ and $\beta \approx 90.3°$) is acquired when sintering is carried out with successive annealing from 1100 °C (48 h) to 800 °C (48 h) in air, then to 650 °C (48 h) in oxygen atmosphere (see Fig. 1(e)) [25].

The reported powder neutron diffraction, the refinement of XRD data and mössbauer study for h-Ba(Ti$_{1-x}$Fe$_x$)O$_{3-\delta}$ suggest that oxygen vacancy merely locates at O(1) randomly [21,26–28]; even in BaFeO$_{2.79}$ [29], the vacancy content at the hexagonally stacked AO$_3$ layers is more than that at the cubic stacked layers. However, structural phase separation deriving from both O(1) and O(2) vacancies is identified in our experiments. As the morphology of as-prepared BTF17 exhibited in Fig. 2(a), two kinds of equivalent amount of grains shaped in particles (<1 μm) and sheets (~10 μm
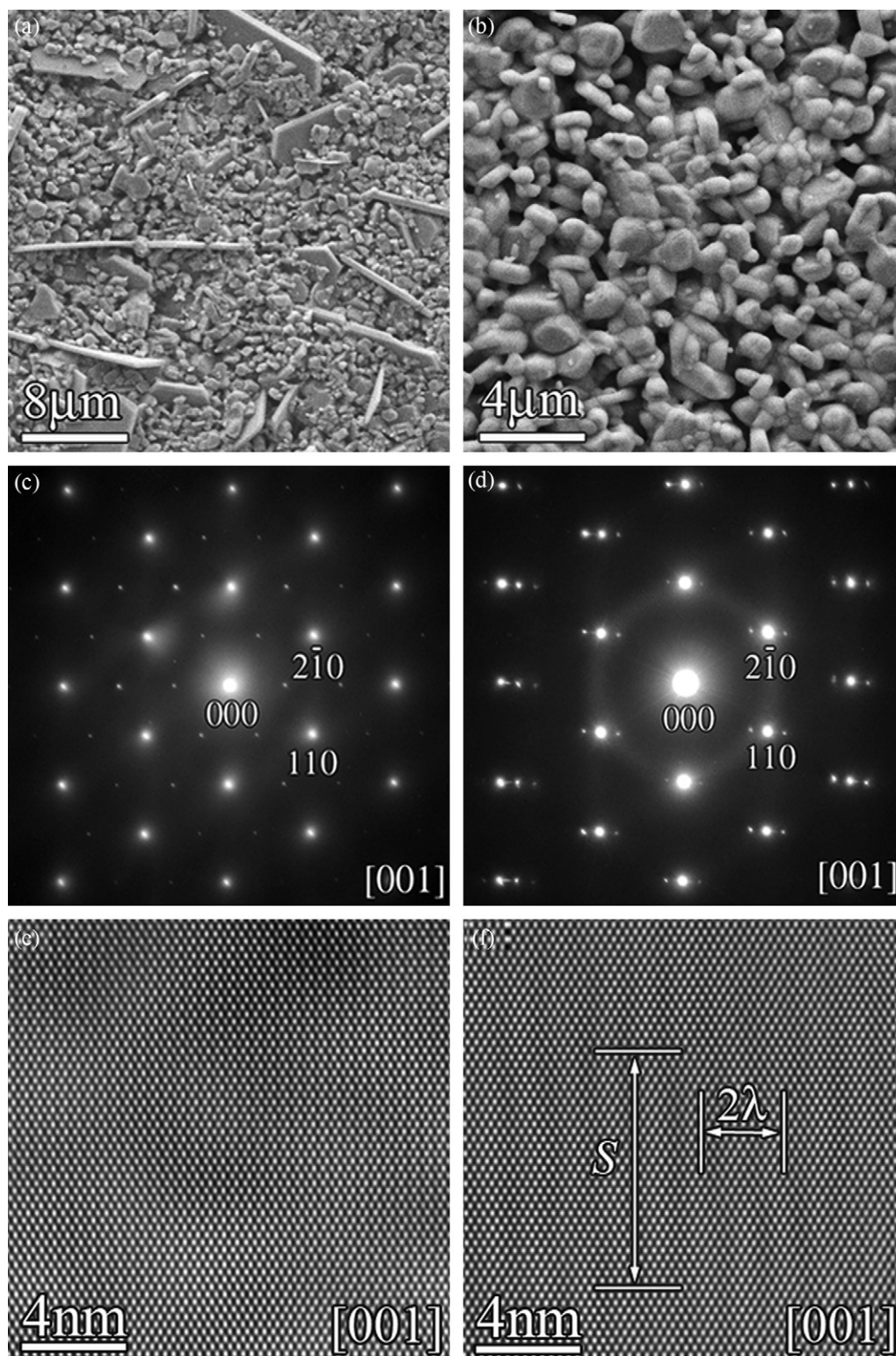
Fig. 2. (a and b) The SEM morphologies of the as-prepared and the post air-annealed BTF17, respectively. (c and d) The ED patterns of the as-prepared BTF17 taken along [0 0 1] zone axis. (e) The corresponding HRTEM image of (c). (f) The corresponding HRTEM image of (d), showing $\lambda = 1.66$ nm, $\alpha \approx 27.02°$ and $S \approx 9$ nm.

in length) are clearly seen. Whereas, uniform particles ranging from 1 to 2 μm are obtained with post-annealing in air (see Fig. 2(b)). In the as-prepared sample, two kinds of structures differentiated from electron diffraction (ED) patterns along [0 0 1] zone axis and related high-resolution TEM images are correspondingly observed. Fig. 2(c) and (e) shows the non-modulated phase (NMP), which pre-serves the six-fold symmetry characteristics of h-BaTiO$_3$. It should

be noted that in the hexagonal compounds with $x < 1/6$, such as BTF10, its structure possesses the non-modulated condition and the vacancy is confined at O(1) only (see Table 1).

Fig. 2(e) and (f) shows the counterbalanced modulated phase (MP), an ICM in the (0 0 1)* plane is featured by modulation wave-length λ, tilting angle α (relative to reciprocal vector $\mathbf{g}_{(110)}$) and domain size S (the distance in real space derived from the splitting
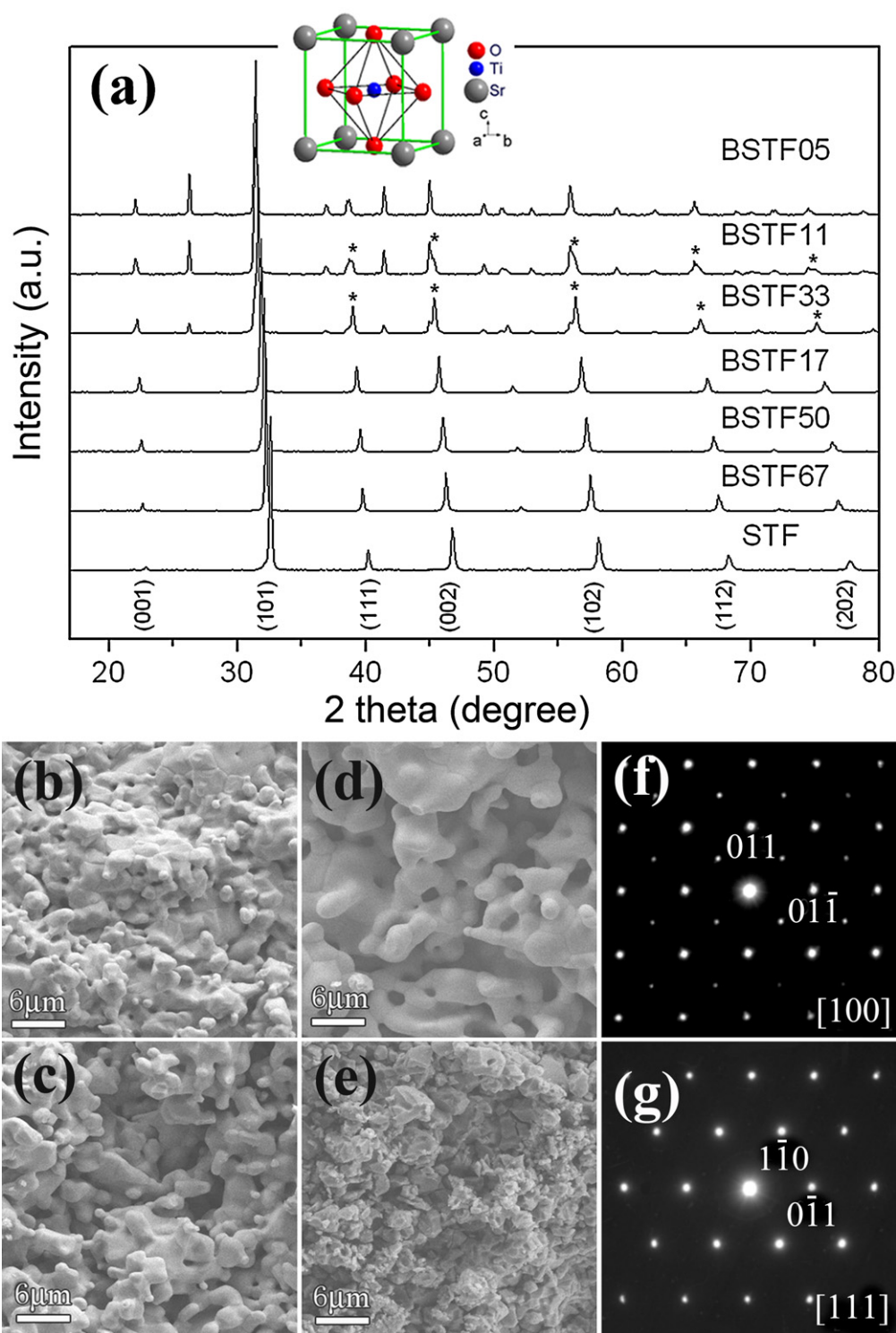
Fig. 3. (a) The XRD patterns of BSTF05, BSTF11, BSTF17, BSTF33, BSTF50, BSTF67 and STF, respectively. The intensity variations of the peaks denoted by the stars in BSTF11 and BSTF17 suggest an enhanced content of the rhombohedral phase in the parent hexagonal polymorph. (b–e) The morphologies of BSTF33, BSTF50, BSTF67 and STF, respectively; their prototype structure $SrTiO_3$ (space group Pm-$3m$) is inserted in (a). (f and g) The ED patterns of BSTF67 along [1 0 0] and [1 1 1] zone axes, exhibiting a pseudo-cubic phase.

satellite spots), which is comparable to a characteristic collective pinning length L_c [30,31]. Post-annealed BTF17 exhibits a uniform ICM, and the XRD refinement suggests that O(2) vacancy simultaneously comes into being associated with the O(1) vacancy (see Table 1). When $x \geq 1/3$, our statistical TEM experiments reveal that the content of NMP decreases sharply and is even negligible as we observed in the as-prepared BTF33 and BTF67, post-annealing in

air can effectively purify the phase separated compounds to be a pure MP, as that happened to BTF17. Therefore, in contrast to the corner-connecting polyhedra in or-BT, the face-sharing octahedra come into being in Fe-doped hexagonal compound, as the schematic crystal structures of o-BT and h-BT shown in Fig. 1(a) and (b). When $x < 1/6$ is doped, the transition from face-sharing to edge-sharing is generated due to O(1) vacancy only, as the case

Table 1
Vacancy condition of partial post-annealed hexagonal $Ba(Ti_{1-x}TM_x)O_{3-\delta}$ ceramics obtained by XRD refinement.

| x	Fe-1/10	Fe-1/6	Fe-1/3	Mn-1/9	Mn-1/6
R_p/R_{wp}	8.97/10.9	14.1/12.7	14.4/11.9	12.9/12.5	13.6/13.1
$V_O(1)$	0.0492	0.0760	0.0404	0.0838	0.1022
$V_O(2)$	0.0	0.0780	0.0620	0.0788	0.0501

Note: V_O denotes oxygen vacancy.

occurred to BTF10. Further Fe doping ($x \geq 1/6$) causes the simultaneous appearances of O(1) and O(2) vacancies and subsequently the amount of bond breaking, as the structural phase separation revealed in BTF17. Correspondingly, the connecting approaches of the polyhedra in hexagonal BTF90 change to point connecting in monoclinic BTF90.

3.2. Hexagonal to pseudo-cubic transition in $(Ba_{1-y}Sr_y)(Ti_{1/3}Fe_{2/3})O_{3-\delta}$ ceramics

Fig. 3(a) shows the XRD patterns of post-annealed $(Ba_{1-y}Sr_y)(Ti_{1/3}Fe_{2/3})O_{3-\delta}$ with doping concentrations of y = 1/18, 1/9, 1/6, 1/3, 1/2, 2/3, 1, which are abbreviated as BSTF05, BSTF11, BSTF17, BSTF33, BSTF50, BSTF67 and STF, respectively. Being similar to BTF67, BSTF05 exhibits a pure hexagonal phase. When doping reaches x = 1/9 (BSTF11) and 1/6 (BSTF17), the content of the secondary rhombohedral phase increases in the parent hexagonal phase. Subsequently, when $x \geq 1/3$, pure perovskite structures with pseudo-cubic polymorph ($a \approx b \approx c \approx 3.96(9)$, 3.94(3), 3.92(3) and 3.88(6) Å; $\alpha \approx \beta \approx \gamma \approx 90°$) for BSTF33, BSTF50, BSTF67 and STF, respectively) are obtained [18,20]. The connecting way between the polyhedra thoroughly transforms into corner sharing in comparison with that in hexagonal BSTF05. The decrease of the cell parameters is seen from the shift of the peaks to higher 2θ values (see Fig. 3(a)). Fig. 3(b)–(e) shows the morphology of the latter four samples, the grain size increases from ∼ 2 to ∼ 6 μm with increasing doping content. However, when Ba is completely substituted, powder-like fragile particles (∼1 μm) possibly resulted from amount of oxygen vacancies and B-site ion mismatch are obtained in STF. As a representative illustration, the ED patterns along [1 0 0] and [1 1 1] zone axes of the pseudo-cubic phase in BSTF67 are presented in Fig. 3(f) and (g), respectively.

3.3. Hexagonal to rhombohedral transition in $Ba(Ti_{1-x}Mn_x)O_{3-\delta}$ ceramics

As an adjacent transition-metal element of Fe, Mn is also doped into $BaTiO_3$ to search for novel multiferroic systems. Hexagonal phases are also obtained in $Ba(Ti_{1-x}Mn_x)O_{3-\delta}$ when x ranges from 1/18 to 1/3 (see Fig. 4(b)). For the Mn-doped case, the stabilization of the hexagonal phase with respect to the doping concentration was discussed a lot [23,32,33], and the reported least amount was x = 2/100 Mn^{4+} [32] (the Shannon ionic radii (IR) [34] are listed in Table 2). In our experiments, the sensitivity of a pure hexagonal phase to valance state is also verified. As depicted in Fig. 4(c), a tetragonal phase as a secondary phase evidently occurs in the post-annealed BTM05. In spite that the as-prepared one is not pure, the preliminary oxidized Mn^{3+} in O_2 atmosphere, in which partial Mn^{4+} comes into being, reduces the content of the secondary phase greatly. The rhombohedral phase becomes counterbalanced in BTM05 sintered in N_2 atmosphere, in which the content of Mn^{3+} is dominant. Thus, the valence state of doped Mn ion plays a crucial role in the formation of hexagonal phase. As we observed in BTF17, TEM experiments reveal that the hexagonal BTM05 and BTM11 are both structurally separated and post-annealing in air can effectively purify the compound to be a uniform MP. When doping concen-
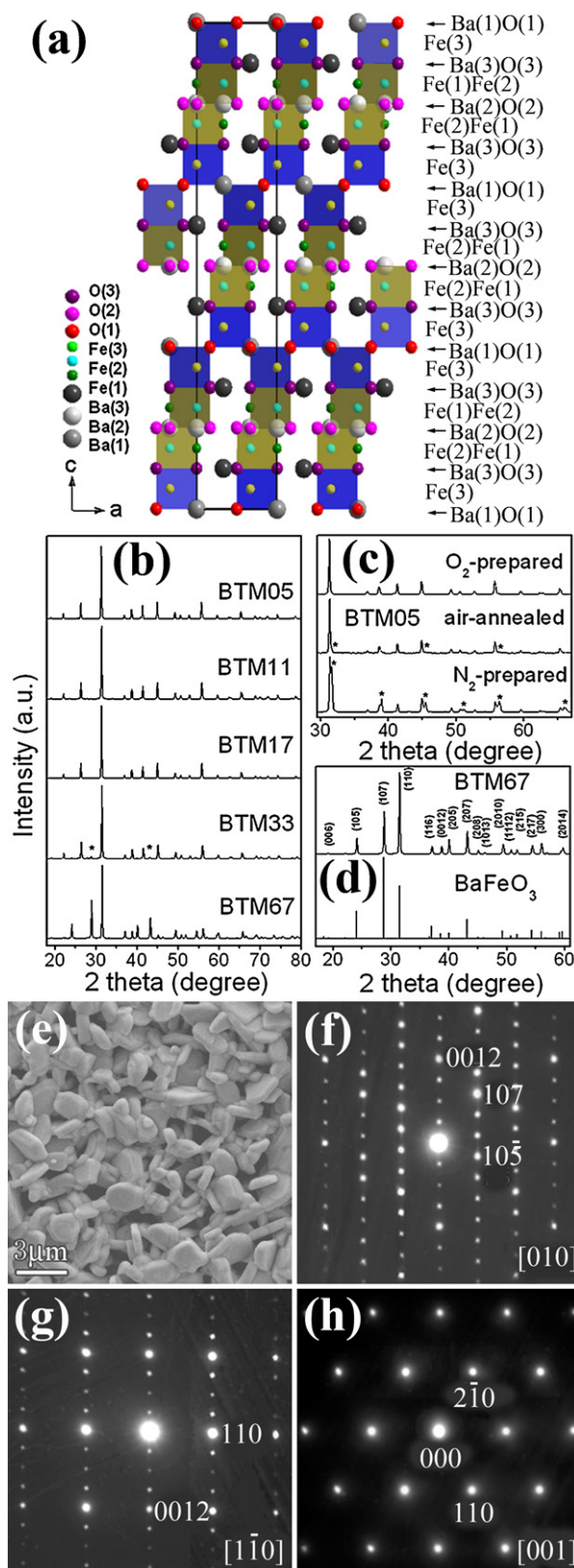
Fig. 4. (a) The crystal structure of $BaFeO_3$ (space group R-$3m$) viewing along [0 1 0] zone axis. (b) The XRD patterns of $Ba(Ti_{1-x}Mn_x)O_{3-\delta}$, which are sintered first at 1000 °C (24 h) in oxygen. (c) The abridged XRD patterns of BTM05 for the as-prepared, the air-annealed at 1200 °C (20 h) and the N_2-prepared (Sintered twice preliminary at 1000 °C (20 h) in N_2 atmosphere and finally air-annealed at 1190 °C (20 h)), respectively. (d) Comparison of the peak profiles of BTM67 and $BaFeO_3$. (e) The morphology of the as-prepared BTM67. (f–h) The ED patterns of BTM67 along [0 1 0], [1 $\bar{1}$ 0], and [0 0 1] zone axes.

Table 2
Effective ionic radii of related atoms with respect to their coordination number (CN) [34].

Ba²⁺ CN	IR (pm)	Sr²⁺ CN	IR (pm)	Ti⁴⁺ CN	IR (pm)	Fe³⁺ CN	IR (pm)	Mn⁴⁺ CN	IR (pm)	Co⁴⁺ CN	IR (pm)
6	135	6	118	4	42	4	49	4	39	4	40
7	138	7	121	5	51	5	58	6	53	6	53
8	142	8	126	6	60.5	6	55	Mn³⁺		Co³⁺	
9	147	9	131	Ti³⁺		Fe²⁺		5	58	6	54.5
10	152	10	136	6	67	4	63	6	64.5	Co²⁺	
11	157	12	144	Ti²⁺		6	61	Mn²⁺		4	58
12	161			6	86			5	66	5	67
								6	75	6	65
								7	67		

Note: The ionic radii of O²⁻ with CN = 2 is 135 pm.

tration increases to $x = 1/3$, a rhombohedral phase is generated in BTM33 (see Fig. 4(b)). Nevertheless, BTM67 shows a pure rhombohedral phase ($a = b = 5.68(1)$ Å, $c = 27.85(4)$ Å; $\alpha = \beta = 90°$, $\gamma = 120°$), which is isostructural with $BaFeO_3$ (Space group $R\text{-}3m$). The coordination of Ti and Mn has changed from the vacancies co-occupied at O(1) and O(2) in h-BTM17 to face-sharing prismatic and corner-connecting polyhedra (see Fig. 4(a)). The strongest peak has been altered because of the co-occupation of Ti and Mn ions at B-site (see Fig. 4(d)). The morphology of the as-prepared BTM67 with grain size of 1–3 μm (see Fig. 4(e)) suggests that BTM67 is a uniform phase, and the ED patterns along [0 1 0], [1 $\bar{1}$ 0] and [0 0 1] zone axes of the rhombohedral structure are shown in Fig. 4(f)–(h).

3.4. Orthorhombic to hexagonal transition in $Ba(Ti_{1-x}Co_x)O_{3-\delta}$ ceramics

As another adjacent transition-metal element of Fe, Co is also doped into $BaTiO_3$. For the substitution of Ti by Co at B-site [19], the doping concentration in hexagonal phase reported by Keith et al. [23] is no more than $x = 1/10$. However, $x = 1/3$ doping is successfully realized in the hexagonal polymorph when sintering is carried out at lower temperature in our experiments. Fig. 5(a) shows the XRD patterns of BTC10 ($x = 1/10$) and BTC33 ($x = 1/3$). The TEM investigations reveal that both BTC10 and BTC33 have a pure MP. Fig. 5(b) and (c) shows the morphology and the [0 0 1] zone axis high-resolution TEM (HRTEM) image of BTC33, respectively. It is found that the sample is crystallized loosely, the ICM depicts the modulation wavelength $\lambda \approx 1.26$ nm and domain size $S \approx 4.1$ nm.

4. Discussion

Generally speaking, the structural transition from the orthorhombic to the hexagonal is observed in Fe, Mn and Co doped $BaTiO_3$. Apart from the different acceptor doping ranges in stabilizing the hexagonal phase at room temperature, among which Fe could be doped most, structural ICM caused by O(1) and O(2) vacancies prevails in the hexagonal system. In spite that the bond breaking will possibly reduce the long-range ferromagnetic interaction, new types of magnetic interactions and the probable relaxor ferroelectricity could be expected due to the nanoscale structural modulation. As the magnetocapacitive coupling revealed in relaxor ferroelectricity and ferromagnetism coexisting $CdCr_2S_4$ [35], in which the ferroic orders develop independently, novel room temperature multiferroics could be expected.

Meanwhile, owing to the oxygen vacancies introduced by acceptor doping, the varied coordination environment of the transition metals may be quite important. As the structural features revealed in multiferroic $DyMn_2O_5$ [16] and $YMnO_3$ [17], the pentahedral $Mn^{3+}O5$ units determine the ferroelectricity of the two compounds. Similarly, ferroelectricity may also be observed in anisotropic BTF10 due to the edge-sharing pentahedra. Being different from

the coordination in the multiferroic perovskites [36] and the above-mentioned hexagonal polymorphs, the compound BTM67 characterized by face-sharing prism connected by corner oxygen atoms is newly discovered, possibly, novel multiferroic behaviors will be presented.

As for the stabilization of the hexagonal phase influenced by transition-metal doping, factors such as (i) oxygen vacancies, (ii) the electronic configuration of the dopant ion, (iii) metal–metal bonding of cations through the face-sharing octahedra, (iv) the tolerance factor $t = (r_A + r_O)/\sqrt{2}(r_B + r_O)$, as well as (v) the Ba/Ti ratio are discussed [23,32,37]. First of all, for the non-doped $BaTiO_3$, the oxygen-deficient h-$Ba(Ti_{1-x}^{4+}Ti_x^{3+})O_{3-x/2}$ obtained by reducing the tetragonal polymorph [38] suggests the simultaneous appearances of oxygen vacancies and partial Ti^{3+}, i.e., one O(1) vacancy in the h-BaO_3 layers causes the transformation from face-sharing octahedra to edge-sharing pentahedra, and the appearance of Ti^{3+} due to the electro-neutral requirement can be well accommodated in the varied coordination environment regardless of the slight increase in the IR of Ti^{3+}. This case is observed in BTF10 (see Tables 1 and 2).

Second, the substitution concentration of Fe^{3+}, Mn^{3+} and Co^{3+} is qualitatively determined by their size differences from the average IR of Ti^{4+} and Ti^{3+}. The IR of the dopants is severely impacted by the initial synthesis conditions as we observed in BTF05 and BTM05. The existence and contribution of Ti^{3+} have rarely been reported and discussed before [4,8,9,21,23,33]. However, this plays an important role in the magnetic and electrical behaviors of the doping system. Generally speaking, the IR of the incorporated trivalent ions is smaller than that of Ti^{3+} even Ti^{4+}, when doping concentration becomes high, the existence of the larger size Ti^{3+} seems to be necessary to hold the hexagonal polymorph. This is consistent with the results of our XRD refinement, where fractional Ti^{3+} usually plays a crucial role in lowering the R values in refinements. Detailed electron energy loss spectrum analysis is in progress. In addition, the structural transitions from the hexagonal to the rhombhedral in Mn-doped case and the hexagonal to the pseudo-cubic in Sr-doped BTF67 demonstrate the dominant role of smaller sizes of the dopants at both A- and B-site in driving the structural transformation.

Fig. 6 shows the doping concentration dependence of a and c in post-annealed $Ba(Ti_{1-x}Fe_x)O_{3-\delta}$ ceramics, a slight contraction of the parameters occurs in contrast to the as-prepared ones. The parameter a generally shrinks with increasing x in our experiments, while the expansion of a extends to $x = 2/3$ then drops in quenched samples [21]. The maximum of c occurs at $x = 1/3$ compared to $x = 2/3$ reported by Grey et al. [21]. Combining with the structural evolutions induced by A- and B-site substitution, from the obtained results we suggest that the effect of metal–metal bonding impacted greatly to the quenched samples [21] is not prominent in our experiments. Additionally, the ICM which possibly does not exist in the quenched samples may be another reason for the discrepancies. In
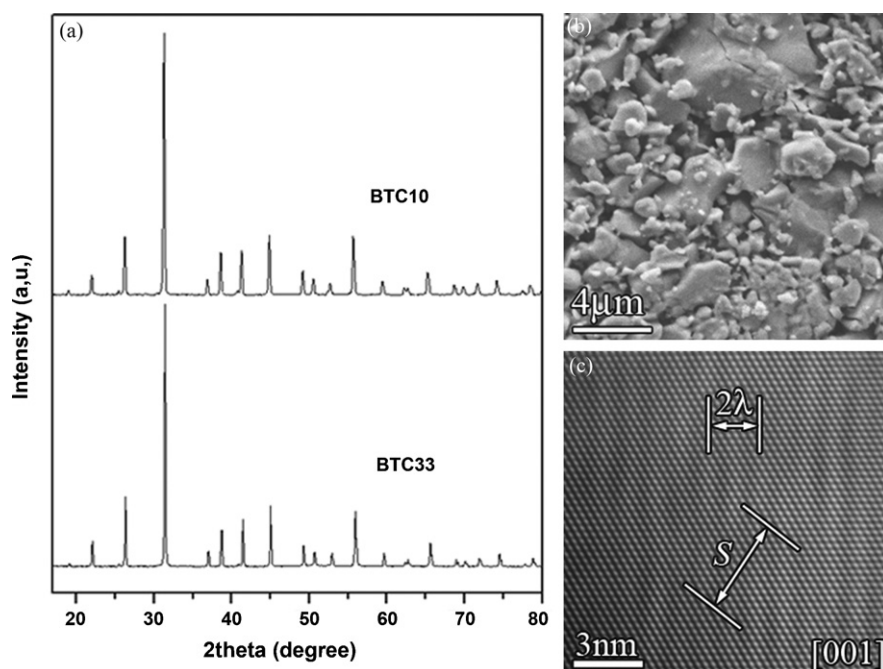
Fig. 5. (a) The XRD patterns of BTC10 and BTC33, the former is sintered in air at 1200 °C (14 h), 1300 °C (20 h), then 1375 °C (6 h), finally 1350 °C (8 h), the latter is sintered twice at 1100 °C (20 h), then annealed at 1000 °C (20 h). (b) The morphology of BTC33; (c) The HRTEM image of BTC33 along [0 0 1] zone axis, the modulation wavelength λ and domain size S are depicted.

a word, the discrepancies between our results and those reported by Grey et al. [21] may be caused by the different synthesis conditions. The structural phase separation may be caused by O(1) and O(2) vacancies and the smaller ion substitution while the contribution of metal–metal bonding is negligible. This is reflected from the structural characteristics of BTF10, BTM11 and BTC10. Therefore, a much wider doping range can be accommodated when the size of the dopant is much closer to Ti ions.

The preparation conditions are merely used to adjust the electronic structure of the dopants and such an effect is prominently manifested in BTF90 where two kinds of polymorphs are obtained when two sintering routes are carried out. The structure evolution from the hexagonal to the monoclinic is greatly affected by the ratio of Fe^{4+}/Fe^{3+} because a much smaller IR can be expected on Fe^{4+} and the structural stability is well compensated when less oxygen vacancies appear. The reported versatile polymorphs of $BaFeO_{3-\delta}$, $BaMnO_3$ and $BaCoO_{3-\delta}$ demonstrate that the IR and the associated electronic structure of the transition metals play determinant roles in phase identification. However, the tolerance factor seems

failed in leveling the expected polymorphs with amounts of oxygen vacancies.

5. Conclusions

Structural transitions from an orthorhombic to a hexagonal phase are all observed in Fe, Mn and Co doped $BaTiO_3$ systems with starting concentrations of ∼1/10. Transitions from a hexagonal to a rhombohedral phase in $Ba(Ti_{1-x}Mn_x)O_{3-\delta}$ and a hexagonal to a pseudo-cubic phase in $(Ba_{1-y}Sr_y)(Ti_{1/3}Fe_{2/3})O_{3-\delta}$ are observed as well. The solubility of the doped metals in $BaTiO_3$ is strongly dependent on the preparation conditions, as we observed in BTF05, BTM05, BTF90 and BTC33. Oxygen vacancies at both O(1) and O(2) as well as the substitution of smaller cations at B-site result in an incommensurate modulation in the hexagonal polymorph, which causes a structural phase separation in Fe-doped case. The size effect of dopants in B-site doped compounds such as BTF10, BTM11 and BTC10 and A-site substituted BTF67 further verifies the influence of ionic radii to structural evolution.
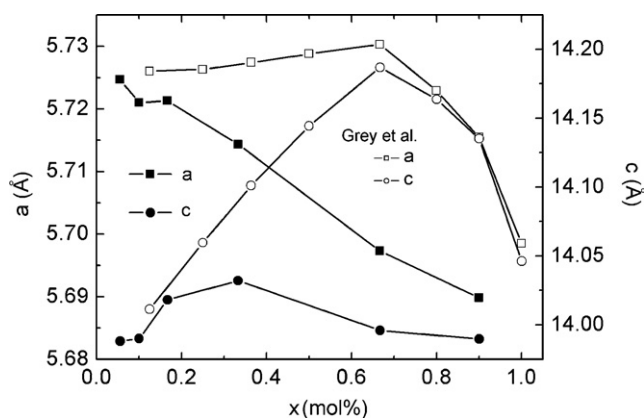
In summary, the oxygen vacancies, smaller cation substitutions of A-site Ba and B-site Ti and thus related electronic configuration variations of elements in the doped matrix are the fundamental driving forces for the structural evolutions. Different coordination of the B-site cations centered polyhedra is obtained in the acceptor doped $BaTiO_3$ system. Detailed investigations on the physical properties of these samples are undergoing.

Fig. 6. The dependence of cell parameters a and c (solid symbols) on doping concentration x in post-annealed $Ba(Ti_{1-x}Fe_x)O_{3-\delta}$ and BTF90, the curves depicted with open symbols are the results of the quenched samples reported by Grey et al. [21].

References

[1] Y.H. Chu, L.W. Martin, M.B. Holcomb, M. Gajek, S.J. Han, Q. He, N. Balker, C.H. Yang, D. Lee, W. Hu, Q. Zhan, P.L. Yang, A. Fraile-Rodeíguez, A. Scholl, S.X. Wang, R. Ramesh, Nat. Mater. 7 (2008) 478.

[2] W. Eerenstein, N.D. Mathur, J.F. Scott, Nature 442 (2006) 756.
[3] J.R. Teague, R. Gerson, W.J. James, Solid State Commun. 8 (1970) 1073.
[4] B. Xu, K.B. Yin, J. Lin, Y.D. Xia, X.G. Wan, J. Yin, X.J. Bai, J. Du, Z.G. Liu, Phys. Rev. B 79 (2009) 134109.
[5] R. Maier, J.L. Cohn, J.J. Neumeier, L.A. Bendersky, Appl. Phys. Lett. 78 (2001) 2536.
[6] T. Matsui, H. Tanaka, N. Fuimura, T. Ito, H. Mabuchi, K. Morii, Appl. Phys. Lett. 81 (2002) 2764.
[7] S. Ray, P. Mahadevan, S. Mandal, S.R. Krishnakumar, C.S. Kuroda, T. Sasaki, T. Taniyama, M. Itoh, Phys. Rev. B 77 (2008) 104416.
[8] F. Lin, D. Jiang, X. Ma, W. shi, J. Magn. Magn. Mater. 320 (2008) 691.
[9] F. Lin, W. Shi, J. Alloys Compd. 475 (2009) 64.
[10] G.-P. Du, Z.-J. Hu, Q.-F. Han, X.-M. Qin, W.-Z. Shi, J. Alloys Compd. 492 (2010) L79.
[11] F. Lin, W. Shi, Phys. B 405 (2010) 1750.
[12] F. Lin, W. Shi, J. Alloys Compd. 495 (2010) 167.
[13] M.S. Tsai, T.Y. Tseng, Mater. Chem. Phys. 57 (1998) 47.
[14] Z. Liu, H. Deng, P. Yang, J. Chu, Mater. Lett. 63 (2009) 2622.
[15] J. Wu, C.-W. Nan, Y. Lin, Y. Deng, Phys. Rev. Lett. 89 (2002) 217601.
[16] D. Higashiyama, S. Miyasaka, N. Kida, T. Arima, Y. Tokura, Phys. Rev. B 70 (2004) 174405.
[17] B.B. Van Aken, T.T.M. Plastra, A. Filippetti, N.A. Spaldin, Nat. Mater. 3 (2004) 164.
[18] N.A. Hill, J. Phys. Chem. B 104 (2000) 6694.
[19] Y. Li, Q. Liu, T. Yao, Z. Pan, Z. Sun, Y. Jiang, H. Zhang, Z. Pan, W. Yan, S. Wei, Appl. Phys. Lett. 96 (2010) 091905.
[20] F. Lin, W. Shi, J. Magn. Magn. Mater. 322 (2010) 2081.
[21] I.E. Grey, C. Li, L.M.D. Cranswich, R.S. Roth, T.A. Vanderah, J. Solid State Chem. 135 (1998) 312.
[22] T.A. Vanderah, J.M. Loezos, R.S. Roth, J. Solid State Chem. 121 (1996) 38.
[23] G.M. Keith, M.J. Rampling, K. Sarma, N.Mc. Alford, D.C. Sinclair, J. Eur. Ceram. Soc. 24 (2004) 1721.
[24] R. Maier, J.L. Cohn, J. Appl. Phys. 92 (2002) 5429.
[25] I.G. Muro, M. Insausti, L. Lezama, T. Rojo, J. Solid State Chem. 178 (2005) 1712.
[26] T.A. Colson, M.J.S. Spencer, I. Yarovsky, Comput. Mater. Sci. 34 (2005) 157.
[27] E. Mashkina, C. McCammon, F. Seifert, J. Solid State Chem. 177 (2004) 262.
[28] I.E. Grey, L.M.D. Cranswich, C. Li, J. Appl. Cryst. 31 (1998) 692.
[29] A.J. Jacobson, Acta Crystallogr. B 32 (1976) 1087.
[30] T. Nattermann, V. Pokrovsky, V.M. Vinokur, Phys. Rev. Lett 87 (2001) 197005.
[31] S. Lemerle, J. Ferré, C. Chappert, V. Mathet, T. Giamarchi, P. Le Doussal, Phys. Rev. Lett 80 (1998) 849.
[32] F. Ren, S. Ishida, S. Mineta, J. Ceram. Soc. Jpn. Int. Ed. 102 (1994) 106.
[33] S.F. Wang, Y.C. Wu, Y.C. Hsu, J.P. Chu, C.H. Wu, Jpn. J. Appl. Phys. 46 (2007) 2978.
[34] R.D. Shannon, Acta Crystallogr. A 32 (1976) 751.
[35] J. Hemberger, P. Lunkenheimer, R. Fichtl, H.-A. Krug von Nidda, V. Tsurkan, A. Loidl, Nature 434 (2005) 364.
[36] I.A. Sergienko, E. Dagotto, Phys. Rev. B 73 (2006) 094434.
[37] S. Jayanthi, T.R.N. Kutty, J. Mater. Sci.: Mater. Electron 19 (2008) 615.
[38] D.C. Sinclair, J.M.S. Skakle, F.D. Morrison, R.I. Smith, T.P. Beales, J. Mater. Chem. 9 (1999) 1327.